

Ref. Ares(2021)5934337 - 29/09/2021

This project has received funding from European Union's Horizon 2020 research and innovation programme under grant agreement No 964588.

## Simulation of High Order Harmonics Generation with Quasi-Phase-Matching strategies

This project has received funding from the European Union's Horizon 2020 research and innovation programme under Grant Agreement No. 964588

Deliverable number: D1.1

Due date: 30/09/2021

Nature<sup>1</sup>: R

Dissemination level<sup>2</sup>: PU

Work Package: WP1

Lead Beneficiary: INCDTIM

Contributing beneficiaries: INCDTIM, POLIMI, CNR

---

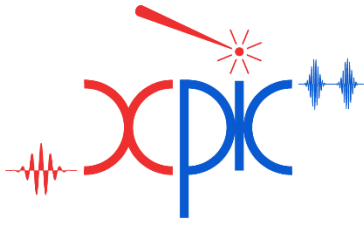
<sup>1</sup> R = Report, P = Prototype, D = Demonstrator, ORDP = Open Research Data Pilot, O = Other, W = Websites, patents filling, etc.

<sup>2</sup> CO = Confidential, only for members of the consortium (including the Commission Services)

PP = Restricted to other programme participants (including the Commission Services)

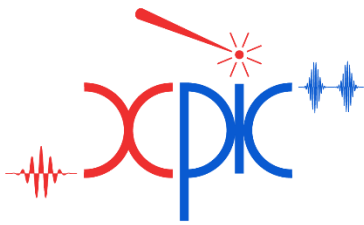
PU = Public

RE = Restricted to a group specified by the consortium (including the Commission Services)



This project has received funding from the European Union's Horizon 2020 research and innovation programme under grant agreement No 964588.

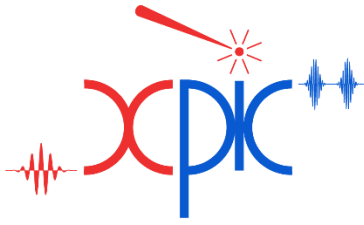
Version	Date	Description
Version 1	28/09/2021	



This project has received funding from the European Union's Horizon 2020 research and innovation programme under grant agreement No 964588.

## Summary

1. Preamble.....	4
2. Modelling macroscopic HHG .....	5
2.1. Modeling laser pulse propagation	6
2.2. Calculating the single-dipole response	8
2.3. Modeling harmonic field propagation	9
2.4. Phase-matching calculation	10
3. Implementation of the pulse propagation method .....	12
4. Testing of the pulse propagation method.....	14
5. Strategies for the QPM in HHG.....	17
5.1. Exploiting gas pressure	17
5.2. Exploiting the gas jets	20
5.3. Exploiting the mode beating	21
5.4. Exploiting the waveguide modulation	23
6. Conclusions.....	26
7. References .....	27

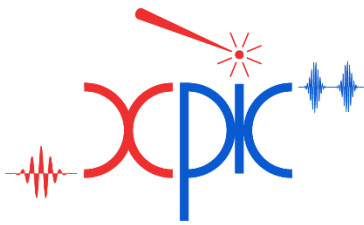


This project has received funding from the European Union's Horizon 2020 research and innovation programme under grant agreement No 964588.

## 1. Preamble

The purpose of this report is to present the results of numerical simulations showing enhancement of High-Order Harmonic Generation (HHG) inside the chip by exploitation of Quasi Phase Matching (QPM) strategies.

The obtained numerical results allowed us to theoretically design the strategies and propose configurations for which QPM is possible inside the chip. However, we have to mention that the feasibility of these configurations will be analyzed, and the selected ones will be subject of practical implementation. This step will be performed by POLIMI, CNR and INCDTIM partners in order to choose the optimal configuration for the final layout of the chip.



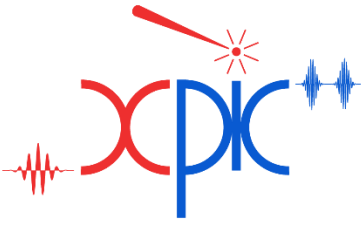
This project has received funding from the European Union's Horizon 2020 research and innovation programme under grant agreement No 964588.

## 2. Modelling macroscopic HHG

The numerical model we will present here follows the physical process as it occurs in real laser-atom interaction systems. The elementary process is the highly nonlinear interaction of the ultra-intense few-cycle laser pulse with one noble gas atom. The basic physical processes behind the formation and propagation of ultrashort light pulses<sup>1</sup> with controlled parameters in hollow fibers include effects related to gas dispersion and dispersion of waveguide modes, self- and cross-phase modulation processes, sum- and difference-frequency generation due to multiwave mixing, high-order harmonic generation, stimulated Raman scattering, as well as processes related to the ionization of the gas filling the fiber.

Due to the fact that the single-atom process takes place in a real macroscopic medium, the complete macroscopic modelling is inevitable. The macroscopic modelling contains the mathematical description and solution of the propagation of laser pulses in ionizing gas medium; the mathematical formulation and numerical solution of the elementary laser-atom interaction in a well-chosen framework of approximation; the propagation of the generated harmonic radiation in the same macroscopic medium; the mathematical formulation and calculation of the phase-matching conditions with the purpose of finding the best possible experimental configuration in order to obtain high harmonic flux.

The elementary process responsible for high-order harmonic generation (HHG) can be understood in the framework of the 3-step model<sup>2</sup>: (1) The electric field of an intense femtosecond laser pulse distorts the Coulomb potential of the noble gas atom, and one active electron can tunnel ionize. (2) The free electron is accelerated under the influence of the laser electric field. During its excursion the electron gains kinetic energy. (3) In the next half optical cycle the electron is driven back to the parent ion and may recombine. The accumulated kinetic energy is released as a high-energy photon. The detectable high-harmonic radiation – which can extend from the XUV to the soft-X-ray spectral domain – is the temporal and spatial coherent sum of the elementary emissions in the given macroscopic medium. However, the efficiency of the whole process is very low mainly due to the very low recombination probability ( $\sim 10^{-5}$ ).



This project has received funding from the European Union's Horizon 2020 research and innovation programme under grant agreement No 964588.

### 2.1. Modeling laser pulse propagation

To build the model<sup>3,4</sup> for free space propagation we assume cylindrical symmetry for the propagation of laser pulses and for the interaction volume where the high-order harmonic generation takes place. Additionally, we consider that the paraxial approximation holds.

The free-space propagation of a laser pulse with electric field  $E_1(r,z,t)$  is described by the Maxwell wave equation:

$$\nabla^2 E_1(r,z,t) - \frac{1}{c^2} \frac{\partial^2 E_1(r,z,t)}{\partial t^2} = \frac{\omega^2}{c^2} (1 - \eta_{eff}^2) E_1(r,z,t) \quad (2.1)$$

Here  $\omega$  is the central angular frequency of the driving field, while  $\eta_{eff}$  is the space- and time-dependent effective refractive index of the medium:

$$\eta_{eff}(n_a, n_e, r, z, t) = \eta_0(n_a) + \eta_2(n_0) I(r, z, t) - \frac{\omega_p^2(n_e, r, z, t)}{2\omega^2} \quad (2.2)$$

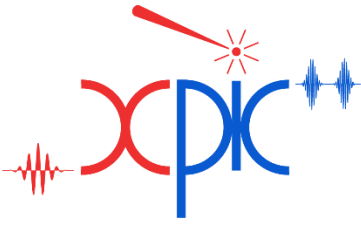
As seen in the expression of the refractive index, it contains three contributions: the first term accounts for the linear refraction and absorption and depends on the density of the neutral atoms  $n_a$ . The second term contains the intensity-dependent nonlinear refractive index which represents the optical Kerr-effect. Here  $n_0$  is the total particle density and  $I(r, z, t)$  is the instantaneous laser intensity. The last term accounts for plasma defocusing, where  $\omega_p$  is the plasma angular frequency,  $n_e$  is the free electron density. Since ionization is the first step during laser-atom interaction, the plasma formation is inevitable in the interaction volume. In most cases this last term dominates the fast variation of the medium's refractive index.

To obtain the solution of the propagation equation we use the so-called moving frame, i.e. transpose the equation in a reference frame moving at speed of light  $c$  together with the laser pulse itself:  $z' = z$  and  $t' = t - z/c$ . The wave equation contains as source term the unknown electric field itself, therefore we implement a self-consistent iterative method for its numerical solution. In order to eliminate the second order derivative in time, the wave equation is Fourier-transformed  $\hat{F}$  and then solved in the frequency domain:

$$\nabla_{\perp}^2 \widetilde{E}_1(r, z', \omega) - \frac{2i\omega}{c} \frac{\partial \widetilde{E}_1(r, z', \omega)}{\partial z'} = \widetilde{G}(r, z', \omega) \quad (2.3)$$

where

$$\widetilde{E}_1(r, z', \omega) = \hat{F}[E_1(r, z', \omega)]$$



This project has received funding from the European Union's Horizon 2020 research and innovation programme under grant agreement No 964588.

and

$$\tilde{G}(r, z', \omega) = \hat{F} \left\{ \frac{\omega_p^2}{c^2} E_1(r, z', t') - 2 \frac{\omega_0^2}{c^2} [\delta_1 + \eta_2 I(r, z', t')] E_1(r, z', t') \right\} \quad (2.4)$$

For propagation in a guided structure the split step method<sup>5</sup> is used to numerically solve the wave equation in frequency domain, in the following way:

1. In the first step we solve the homogeneous equation which contain the diffraction term:

$$\nabla_{\perp}^2 \tilde{E}_1(r, z', \omega) - \frac{2i\omega}{c} \frac{\partial \tilde{E}_1(r, z', \omega)}{\partial z'} = 0$$

At this point the boundary conditions imposed by the hollow core fiber have to be considered, therefore the solution of the homogeneous equation is defined as the superposition of the hybrid EH eigenmodes<sup>6</sup> in the form:

$$\tilde{E}_1(r, z', \omega) = \sum_j b_j(z', \omega) J_0(u_{1j} r/a) \exp(i \int_0^{z'} \gamma_j(z) dz) \quad (2.5)$$

where  $u_{1j}$  are the roots of the Bessel function of the first kind  $J_0$ ,  $a$  is the inner radius of the fiber, while the other quantities are defined as:

$$\gamma_{1j} = \kappa_j - \frac{1}{2\kappa_j} \left( \frac{u_{1j}}{a} \right)^2 - i \frac{1}{2\kappa_j} \left( \frac{u_{1j}}{a} \right)^2 \cdot \frac{2\nu_{1j}}{\kappa_j a} \quad (2.6)$$

being the complex propagation constant, and

$$b_j(z=0) = \frac{2}{a^2 J_1^2(u_{1j})} \int_0^a r J_0 \left( u_{1j} \frac{r}{a} \right) E_1(r) dr \quad (2.7)$$

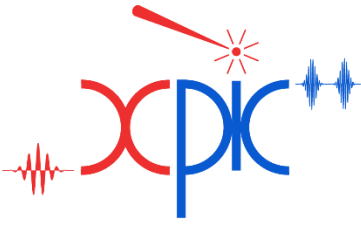
is the coefficient in the development.

If we write  $E_1(z+\Delta z)$  using expression 2.5 and take into account the orthonormality of the Bessel function we obtain an expression which helps us advancing the solution for  $E_1$  by recalculating the new coefficients  $b_j$  as:

$$b_j(z' + \Delta z') = b_j(z') \cdot \exp(\kappa_j \Delta z' - \alpha_j \Delta z') \quad (2.8)$$

Where  $\kappa_j = \frac{\lambda}{4\pi} \left( \frac{u_{1j}}{a} \right)^2$  is the real part of the propagation constant in the moving frame, and

$$\alpha_j = \left( \frac{u_{1j}}{2\pi} \right)^2 \frac{\lambda^2}{a^3} \frac{(n_x^2 + 1)}{2\sqrt{n_x^2 - 1}}$$



This project has received funding from the European Union's Horizon 2020 research and innovation programme under grant agreement No 964588.

is the mode loss term, and  $n_x(\omega_j) = \frac{n_{glass}(\omega_j)}{n(\omega_j)}$  is the ratio of the refractive indices of the dielectric and gas media.

After finding the new coefficients, we rebuild  $E_1(\omega)$ :

$$\widetilde{E}_1(r, z' + \Delta z', \omega) = \sum_j b_j(z' + \Delta z', \omega) J_0(u_{1j} r/a) \quad (2.9)$$

Here we must mention that the coefficients  $b$  are in fact dependent not only on mode index but also on frequency index, and this is an improvement with respect to what is reported in the literature.

2. In the second step we solve the non-homogeneous ordinary differential equation of the form:

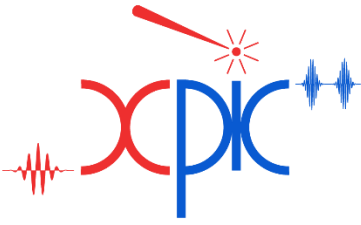
$$-\frac{2i\omega}{c} \frac{\partial \widetilde{E}_1(r, z', \omega)}{\partial z'} = \widetilde{G}(r, z', \omega) \quad (2.10)$$

We use a self-consistent iterative method for the solution which consists in the following procedure:

- (1) The field  $E_1(r, z', \omega)$  obtained as a result of the homogeneous equation is transformed in time domain  $E_1(r, z', t)$ ;
- (2) from  $E_1(r, z', t)$  we calculate  $G(r, z', t)$ ;
- (3) Fourier-transform it into the frequency domain to obtain  $G(r, z', \omega)$ . This latter being the source term for the non-homogeneous ODE,
- (4) calculate the new  $E_1(r, z', \omega)$  and new  $E_1(r, z', \tau)$ .
- (5) If the input (1) and output (4) functions  $E_1(r, z', \omega)$  differ less than a preset tolerance, we consider that convergence has been reached. Otherwise repeat the iteration from step (1) with the input function now being the  $E_1(r, z', \omega)$  obtained after step (4).

## 2.2. Calculating the single-dipole response

The computationally most demanding part of the numerical modeling is to calculate the elementary response in a laser-atom interaction. The accurate treatment of this problem is by solving the time-dependent Schrödinger equation. However, in most experimentally relevant cases several approximations are valid. The strong-field approximation (SFA) which we rely on considers that the ionized electron moves in the continuum solely under the influence of the driving field; only the ground state is taken into account both at the ionization and recombination



steps<sup>7</sup>. With these approximations the nonlinear dipole can be calculated by solving the Lewenstein integral. The macroscopic response of the system which is the nonlinear polarization follows from the dipole by including the ionization rate and the ground state depletion:

$$P_{nl}(t) = 2Re \left\{ i \int_{-\infty}^t dt' d^* [p_{st}(t', t) - A(t)] \cdot E_1(t') \exp \left[ - \int_{-\infty}^{t'} w(t'') dt'' \right] \exp[-iS_{st}(t', t)] \cdot d[p_{st}(t', t) - A(t')] \right\} \cdot [n_0 - n_e(t)], \quad (2.9)$$

with  $A$  vector potential,  $p_{st}$ ,  $S_{st}$  stationary momentum and phase,  $d$  bound-continuum transition matrix element,  $w$  ionization rate.

The physical meaning of this expression is as follows: at time  $t'$  the electron appears in the continuum, during its excursion accumulates phase ( $S_{st}$ ) while it moves driven by the laser pulse  $E_1$ , then at time  $t$  it recombines with the parent ion. The accurate solution requires a fine time resolution, which makes the calculations resource consuming.

In our numerical model laser pulse propagation and dipole calculation are linked, so that in every spatial  $(r, z')$  grid point within the interaction volume we calculate the dipole response under the influence of the recently modified laser electric field. In this way the propagation effects are taken into account during the laser-atom interaction. This capability is the strong part of the model and makes it suitable to reproduce real experimental results.

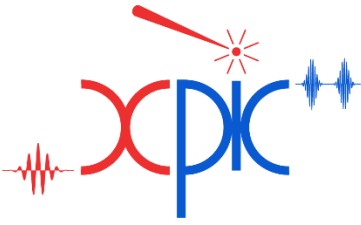
### 2.3. Modeling harmonic field propagation

The dipole radiations emitted at different times during the driving pulse and in different spatial points propagate in the same medium together with the driving pulse. The macroscopic harmonic field is the coherent superposition of the elementary emissions.

The  $P_{nl}$  nonlinear polarization is the source for the harmonic propagation, therefore the wave equation for the harmonic field has the form:

$$\nabla^2 E_h(r, z, t) - \frac{1}{c^2} \frac{\partial^2 E_h(r, z, t)}{\partial t^2} = \mu_0 \frac{\partial^2 P_{nl}(r, z, t)}{\partial t^2} \quad (2.11)$$

While this equation is very similar to that describing the driving pulse propagation, there are two major differences which both make it simpler to solve. First, the source term is known, therefore iterative method is not needed. Second, the resulting XUV radiation has very low divergence, it propagates close to the optical axis and does not reach the walls of the fiber. For this reason at



This project has received funding from the European Union's Horizon 2020 research and innovation programme under grant agreement No 964588.

this stage of the implementation we do not need to consider fiber propagation modes, but only free-space propagation. Equation (2.11) for harmonic propagation is solved in frequency domain for each spectral component, while taking into account dispersion and absorption due to neutrals in the medium through the complex refractive index.

At the exit of the interaction volume, i.e. the fiber in this case, we consider the “near-field” and the relevant results of the calculations are given. These are the driving pulse’s temporal, spectral and spatial profile, the high-harmonic power spectrum, spatial / temporal / spectral evolution of selected spectral components and/or domains.

After leaving the interaction region the harmonic field propagates in vacuum until the “far-field” which can be a detector or a second interaction chamber for the further application of the XUV radiation. The Hankel transform describes the transport from the near-field to the far-field through linear optical elements represented by the  $\begin{pmatrix} A & B \\ C & D \end{pmatrix}$  ray matrix:

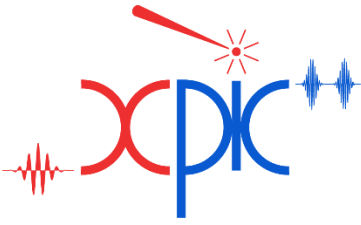
$$E_{\omega}(r, z) = -\frac{2\pi}{\lambda B} \exp\left[ik\left(z + \frac{Dr^2}{2B}\right)\right] \int_0^a E_{\omega}(r_1, z_1 = 0) \exp\left(\frac{ikAr_1^2}{2B}\right) J_0\left(\frac{krr_1}{B}\right) r_1 dr_1 \quad (2.12)$$

#### 2.4. Phase-matching calculation

The macroscopic high-harmonic radiation which can be detected after the interaction region (in the near- and/or far-field) is the result of the coherent superposition of the elementary dipole emissions all through the interaction volume  $(r, z')$  as they are generated in successive optical cycles of the driver (temporal aspect) and as they propagate in the gas medium (spatial aspect). As a general and simple term we use “phase-matching”, but it depends on all experimental parameters of the HHG process, such as the laser pulse characteristics (wavelength, duration, intensity, focusing geometry), the medium properties (gas type, pressure, interaction length and its position relative to the laser focus).

The basic phase-matching model has been formulated by Balcou<sup>8</sup>. The condition for perfect phase-matching is obtained when the wavevector of the  $q^{\text{th}}$  order harmonic  $\mathbf{k}_q$  equals the dipole wavevector  $\mathbf{k}_{\text{pol}}$ :

$$\mathbf{k}_q = \mathbf{k}_{\text{pol}} = q \left( (2\pi/\lambda) \mathbf{e}_z + \nabla \varphi_{\text{Gouy}}(r, z) \right) + \nabla \Phi_{\text{at}}(r, z)$$



This project has received funding from the European Union's Horizon 2020 research and innovation programme under grant agreement No 964588.

The dipole's wavevector has two components: the first term is the wavevector of the driving field ( $\mathbf{k}_1$ ) and the second term is the gradient of the atomic phase accumulated by the electron during its excursion in the laser field ( $\mathbf{K}$ ). The driving field's wavevector in turn contains the phase variation due to geometrical focusing (Gouy phase). At this point our phase-matching model introduces a generalization in order to be able to include the propagation-induced laser pulse distortions into the calculations. Namely, the wavevector of the driving field is calculated from the phase gradient of the *propagated* solution of the driving field ( $E_1(r, z', t)$ ) i.e. the result from section 2.1) taking into account the self-phase modulation. Based on the same principle, also the atomic wavevector is calculated from the *propagated* solution of  $E_1(r, z', t)$  by averaging over one optical cycle. Finally, in our model the phase-matching condition has the following expression:

$$\mathbf{k}_q(r, z, t) = \mathbf{k}_{pol}(r, z, t) = q \left\{ \left( \frac{2\pi}{\lambda} \right) \mathbf{e}_z + \nabla \arg[E_1(r, z, t)] \right\} + \nabla \alpha \bar{I}(r, z, t)$$

In real HHG configurations one never has perfect phase-matching. However, there is a practical rule which we can use in order to optimize phase-matching within the given experimental parameter range. We can calculate the phase-mismatch as:

$$\delta k(t) = q \frac{2\pi}{\lambda} - |\mathbf{k}_{pol}(t)|$$

and from here we define the coherence length ( $L_{coh}$ ) as the distance over which the phase varies by pi:

$$L_{coh}(t) = \frac{\pi}{\delta k(t)} \quad (2.12)$$

As a general practical guide we consider that a given harmonic order is generated under good phase-matching conditions if its coherence length is comparable to the medium length.

### 3. Implementation of the pulse propagation method

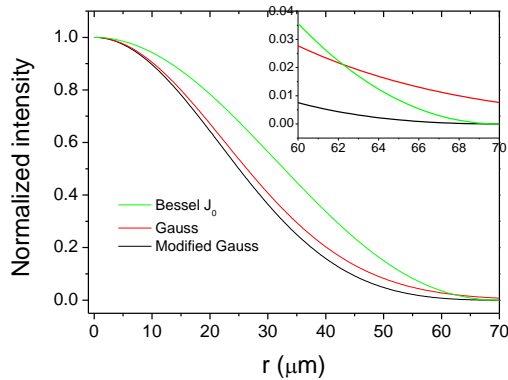


Fig. 3.1 Three radial profiles for the input beam, as used in the modeling for a 140 μm fiber

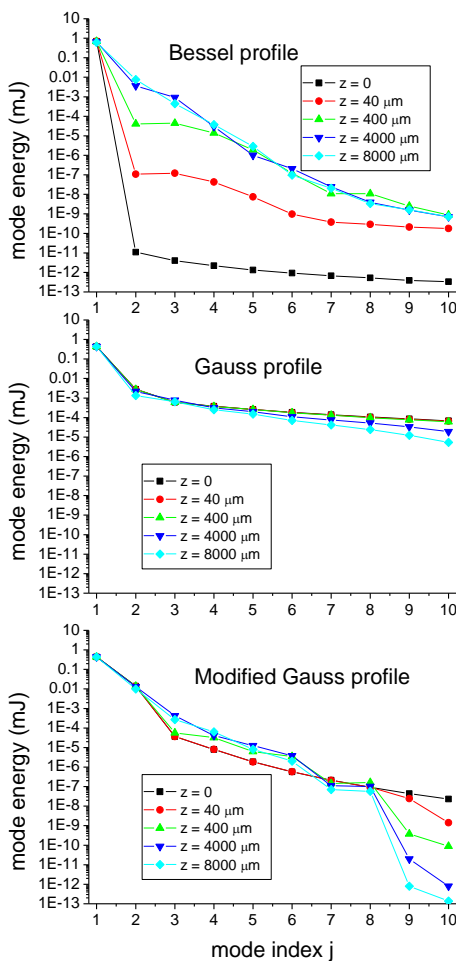


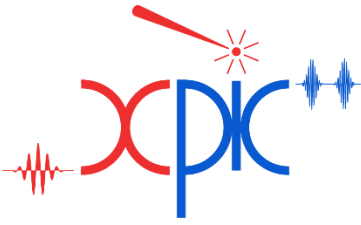
Fig. 3.2 Energies of the  $E_{1j}$  modes for the initial profiles and for different propagation distances

The code was written in F90 following the method described in the preceding section. In this section we will outline the main features and technical challenges of the work. Then the code was tested against experimental data found in the literature, and the results obtained will be presented.

A first task was to determine the *number of modes* used to describe the ultrafast field inside the channel. The criterion for establishing this number was set initially the amplitude of each mode but then the energy contained in each mode proved to be a good criterion.

A second parameter to choose was the initial radial profile of the laser beam. As will be illustrated later this choice will influence the weight of each mode and will give rise to mode beating during propagation.

Given in Fig. 3.1 is the radial profile for three cases which were investigated: i) the Bessel  $J_0$  profile (used by most of the simulations in the reported literature because of better convergence), ii) the Gauss profile with a waist  $w$  calculated from the channel radius  $a$ , as being  $w=0.64*a$  to give the best coupling of the beam with the channel, and iii) a modified Gauss which is the Gauss profile with the same waist but shifted down in intensity so that at the channel wall the field is zero. The inset shows better the difference between the three cases. One has to note that at equal intensities the energy contained in the Bessel profile is higher (by about 32%) than that contained in the Gauss profile. This is important in calculating the initial peak intensity because pulse energy is an experimental value



which must be taken into account.

The number of modes necessary to be taken into account will depend on the initial beam profile. We show in Fig. 3.2 the energies contained in the first 10 modes for the three radial profiles and as a function of propagated distance along the channel. The Bessel profile needs fewer modes as the initial field is entirely contained in the  $E_{11}$  mode. As propagation advances higher modes will be populated but even after 8 mm of propagation the energy contained in  $E_{12}$  mode is less than 1%. For the Gauss profile higher modes contain significantly larger amounts of energies while the modified Gauss profile will have an intermediary behavior. In this case the decrease of the mode energies is similar to the Gauss profile up to  $E_{18}$  mode but falls more abruptly for higher order modes. Based on these results, to be on the safe side, we kept for all simulations a number of 10 modes in describing the propagated field, regardless of the radial profile chosen.

Another difficult task proved to be calculating the  $b$  coefficients using Eq.2.7. The integral exhibits large oscillations of the integrand, and the calculation using traditional numerical methods (including those adapted for fast oscillating functions) did not reduce the errors which in some cases are larger than the value of the integral.

The solution we found is based on a property<sup>9</sup> of  $J_0$  functions. We start from an integral as

$$g(y) = 2\pi \int_0^{\infty} E(r)J_0(2\pi N_f y r) r dr$$

and we have for the particular case  $y=1$ ., then  $g = 2\pi \int_0^{\infty} E(r)J_0(2\pi N_f r) r dr$

If  $E$  is a Heaviside function, that is

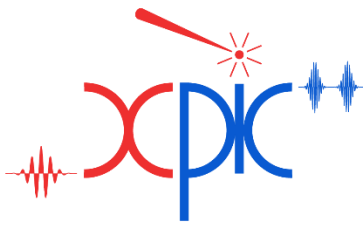
$$E(r) = f(x) = \begin{cases} 1, & 0 < r < a \\ 0, & \text{otherwise} \end{cases}$$

then  $g = aJ_1(2\pi a N_f)/N_f$

If we consider a sub-interval  $\zeta_n < x_n < \zeta_{n+1}$  in which  $E$  is constant one obtains:

$$\int_{\zeta_n}^{\zeta_{n+1}} E(r)J_0\left(\frac{\mu_i}{a}r\right) r dx = \frac{E(x_n)}{\frac{\mu_i}{a}} \left[ \zeta_{n+1}J_1\left(\frac{\mu_i}{a}\zeta_{n+1}\right) - \zeta_nJ_1\left(\frac{\mu_i}{a}\zeta_n\right) \right]$$

We implemented this method on the  $r$  scale and took  $\zeta_n$  grid points as being overlapped on the chosen grid for the  $r$  coordinate. A side benefit of developing this method is that it can be applied for calculating the harmonic far field from the near field. Indeed, we found that the Hankel transform (see Eq.2.12) used to transport the near field into the far field involves the calculation of the same kind of integral, and this exhibits the same oscillations as in the case of  $b$  coefficients calculation.



This project has received funding from the European Union's Horizon 2020 research and innovation programme under grant agreement No 964588.

#### 4. Testing of the pulse propagation method

These preliminary steps in the development were necessary to ensure the correctness of the method implementation. However, we looked for a test case of the method, preferably against experimental data or similar modeling of the propagation equation using different method of solving. Both cases were found in the literature and we present here the results of these two tests.

In the experiment, a 40 fs laser pulse at 790 nm central wavelength was focused into a 70 mm long capillary of 140  $\mu\text{m}$  diameter, using a lens of  $f=70$  cm. In this configuration  $w/a=0.64$  thus an ideal coupling between the Gaussian beam and the fiber. The authors report a scan along the propagation coordinate of the visible emission from the ionized argon. The results can be seen in Fig.3.3.

We simulated similar experimental condition. In particular we consider a 5 cm long capillary with a 75  $\mu\text{m}$  radius hole filled with argon at a pressure of 80 mbar in the central part of the capillary; the Ar pressure increases over 3 mm from 0 to 80 mbar at the fiber input. Laser pulses of 0.5 mJ energy, and 40 fs duration at 800 nm wavelength are focused with a 40 cm focal length element producing a Gaussian waist of 48  $\mu\text{m}$  (thus  $w/a=0.64$ ) and an initial peak intensity of  $3.8 \times 10^{14}$  W/cm<sup>2</sup>. During propagation we are able to calculate the total electron concentration by integrating along radial direction the electron density. The result is plotted in Fig.3.4.a, along with the pulse energy dependence on propagation in Fig.3.4.b. Two ionization models were used, the classical Ammosov-Delone-Krainov (ADK) model<sup>10</sup> and the barrier suppression model<sup>11</sup> which yields higher ionization rates thus a higher electron density. As one can see from comparing Fig. 3.3 and Fig.3.4 the agreement with experimental data is very good for the ADK model, both in the positions of the maxima and in the splitting of the second and third.

Using an ionization model with higher ionization rates is similar to using a higher gas pressure, because both create a larger electron density. The effect on plasma is to increase the fluorescence yield but also enhance the intensity modulation along propagation. Of course the pulse energy during propagation will suffer higher losses due to higher ionization.

Another comparison was made against modeling the same experimental data by solving a nonlinear Schrodinger equation<sup>12</sup>, thus a different numerical method. The results, reported in<sup>13</sup> are shown in Fig.3.5.

All three sets of data agree well between each other. This agreement practically validates our model and we are entitled to use it in modeling pulse propagation and harmonic generation in the waveguide. The data show a periodic modulation of the plasma density along the propagation direction, which was explained as being the result of mode beating. Indeed, a Gaussian beam radial profile cannot be described well by only the lowest order mode  $E_{11}$ . Higher modes like  $E_{12}$  and  $E_{13}$  will take part even in the case of an optimal coupling between the beam and the fiber.

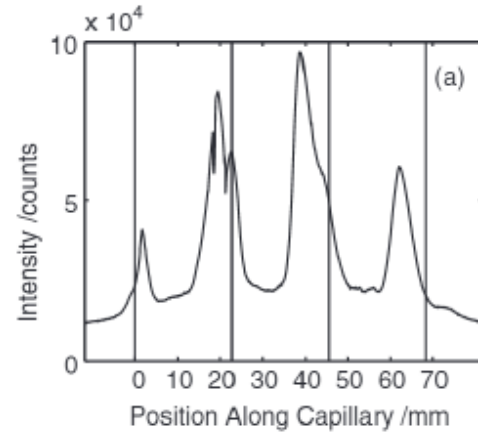
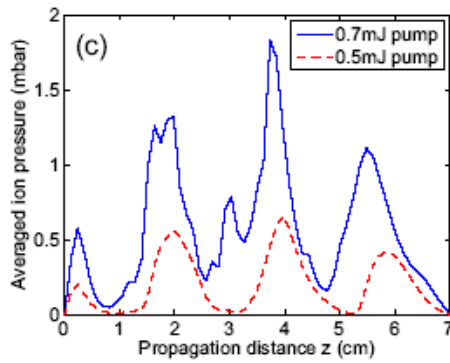


Fig.3.3 Measured emission of Ar neutral species along propagation. The vertical lines show the theoretical positions of the beating between the two lowest modes  $E_{11}$  and  $E_{12}$

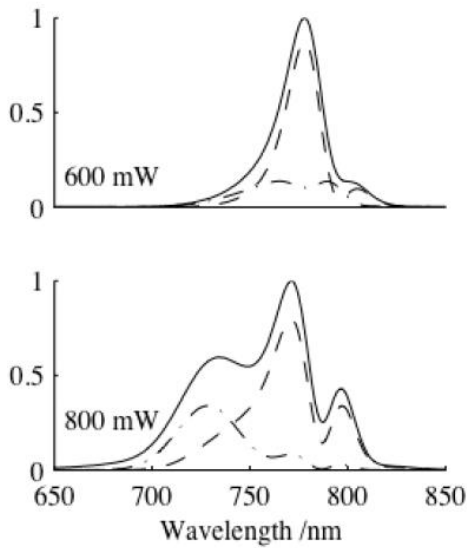


Fig.3.5 Modeling the experimental data using the nonlinear Schrodinger equation reported in Opt. Ex. 18, 13279 (2010). Two pulse energies and average power are mentioned in the captions.

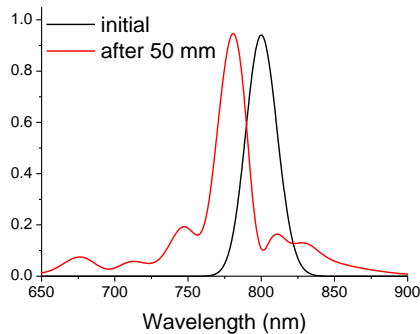


Fig. 3.6 Normalized spectral profiles on-axis

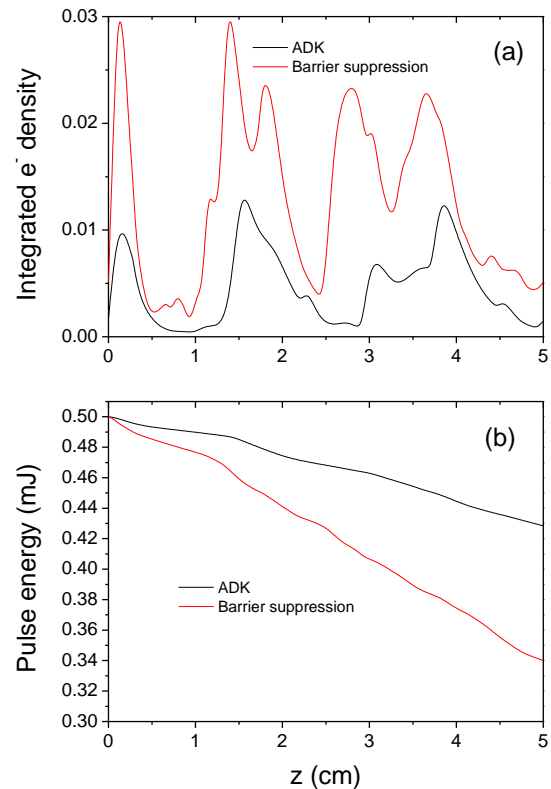


Fig.3.4 Total electron density (a) and pulse energy (b) as a function of  $z$  position along the HCW, for two ionization models, as detailed in the text.

These modes will interfere during propagation giving rise to the beating seen in Fig. 3.3-3.5. This is the basic phenomenon but ionization will also influence the period of these modulations, as shown in Fig. 3.3, where the vertical lines indicate the theoretical positions of the beating between  $E_{11}$  and  $E_{12}$  which differ from the actual positions and show a shorter distance of the period.

The influence of ionization can be seen the spectra of the propagated field shown in Fig.3.5 for 600 mW and 800 mW average power. The blue shift is present and the wings are attributed<sup>13</sup> to the higher modes. Our results, shown in Fig.3.6 exhibit the same characteristics. The on-axis time profile shows the split of the pulse while the spectral profile shows the blue-shift and the wings.

In closing this section we show in Fig 3.7 (left) the spatial configuration of the peak intensity and (right) the evolution of the energies of the first three modes along the propagation direction. The spatial configuration reveals the mode beating in a more clear way but confirms the fluorescence

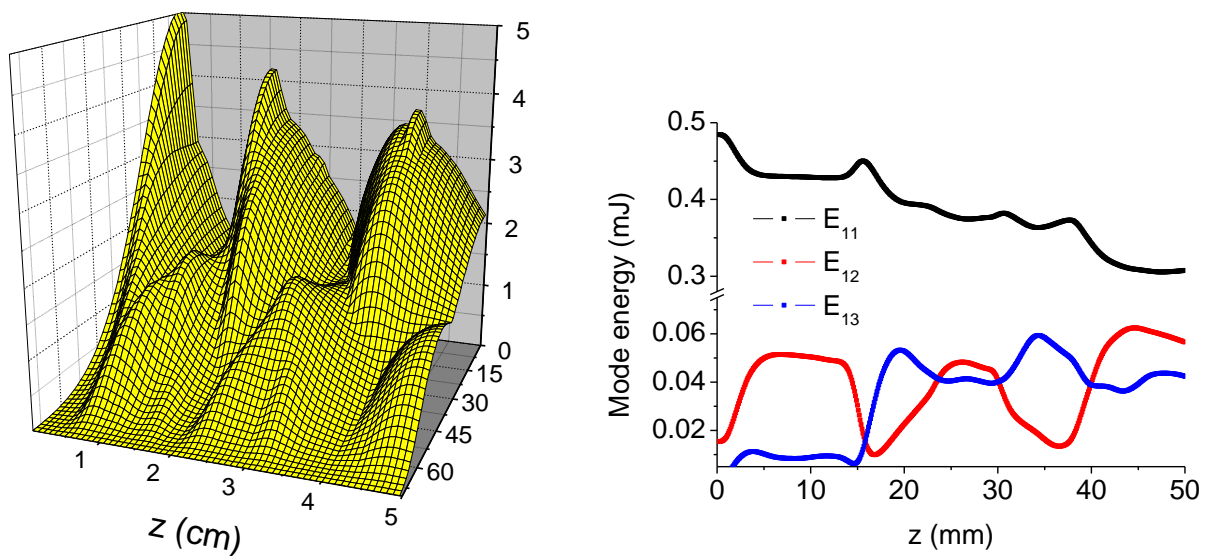


Fig.3.7 The spatial configuration of the peak intensity (left) and (right) the evolution of the first three mode energies during propagation.

evolution along the propagation direction. The evolution of the mode energies of the first three modes clearly shows that the exchange of energy between  $E_{11}$  and  $E_{12}$  dominates the initial part, but after 15 mm  $E_{13}$  also plays a role comparable with the  $E_{12}$ .



This project has received funding from the European Union's Horizon 2020 research and innovation programme under grant agreement No 964588.

## 5. Strategies for the QPM in HHG

The results which will be presented further on, have as main goal to establish the strategies for Quasi-Phase-Matching (QPM) in the process of high harmonic generation in a waveguide filled with a noble gas. The main parameters we consider here are the gas pressure, the distribution of the gas pressure in the waveguide, the length of the guided propagation, the modulation of the waveguide diameter, and the driving pulse characteristics like wavelength, energy, duration and initial radial profile which will determine initial intensity and initial ionization level. We focused on two driving wavelength, 800 nm and 2000 nm taking into account the laser systems which are and respectively will be available in the laboratory.

### 5.1. Exploiting gas pressure

As a first introductory step we can consider a simple model<sup>14</sup> for the wavevector mismatch between the fundamental pulse and the  $q$ -th harmonic which is due to the waveguide, plasma and neutral atoms

$$\Delta k = k_{q\omega} - qk_{\omega} = \frac{qu_{11}^2\lambda}{4\pi a^2} + P\eta N_{atm}r_e \left( q\lambda - \frac{\lambda}{q} \right) - \frac{2\pi(1-\eta)Pq}{\lambda} \left[ \delta(\lambda) - \delta\left(\frac{\lambda}{q}\right) \right] \quad (5.1)$$

where  $q$  is the order of the harmonic generated by a laser field of frequency  $\omega$  and wavelength  $\lambda$  while  $a$ ,  $u_{11}$ ,  $\eta$ ,  $P$ ,  $N_{atm}$ ,  $r_e$  and  $\delta$  are the waveguide radius, first zero of Bessel function  $J_0$ , ionization fraction, gas pressure in atmospheres, number density at 1 atm, classical electron radius and index of refraction of the neutral gas at 1 atm, respectively.

For low pressures or high ionization fraction ( $\eta$  close to unity) the last term of the above equation can be neglected and one has

$$\Delta k = \frac{qu_{11}^2\lambda}{4\pi a^2} + P\eta N_{atm}r_e \left( q\lambda - \frac{\lambda}{q} \right)$$

In the usual case when  $q\lambda \gg \lambda/q$  we can write

$$\Delta k \approx \frac{qu_{11}^2\lambda}{4\pi a^2} + \frac{qn_e e^2 \lambda}{4\pi m_e \epsilon_0 c^2}$$

where  $n_e$  and  $m_e$  are the electron density and electron mass respectively. According to this equation in specific conditions the dominant term is due to electron plasma which is pressure dependent and intensity dependent.

The results of such simple model are well known in the literature<sup>14</sup> and we used them as starting points for modeling. For example for the case of very low ionization the optimal gas pressures for the generation of harmonic order 27 (780 nm) in He, Ne, Ar, Kr, and Xe are around 130, 75, 20, 14, and 8 Torr respectively, if a waveguide with 150  $\mu\text{m}$  diameter is used.

The inclusion of ionization changes dramatically this picture. The inclusion of only 1% of ionization have influence on the pulse phase and amplitude and in these practical cases one has to use more sophisticated models to find the driving field configuration over the whole interaction region and after that to find the phase matching conditions and the generated harmonic field.

Following the waveguide configuration the gas density along the channel was calculated (using COMSOL) and used further in HHG simulations. The spectra shown in Fig. 5.1 and 5.2 are calculated following the procedure described in Sec. 2

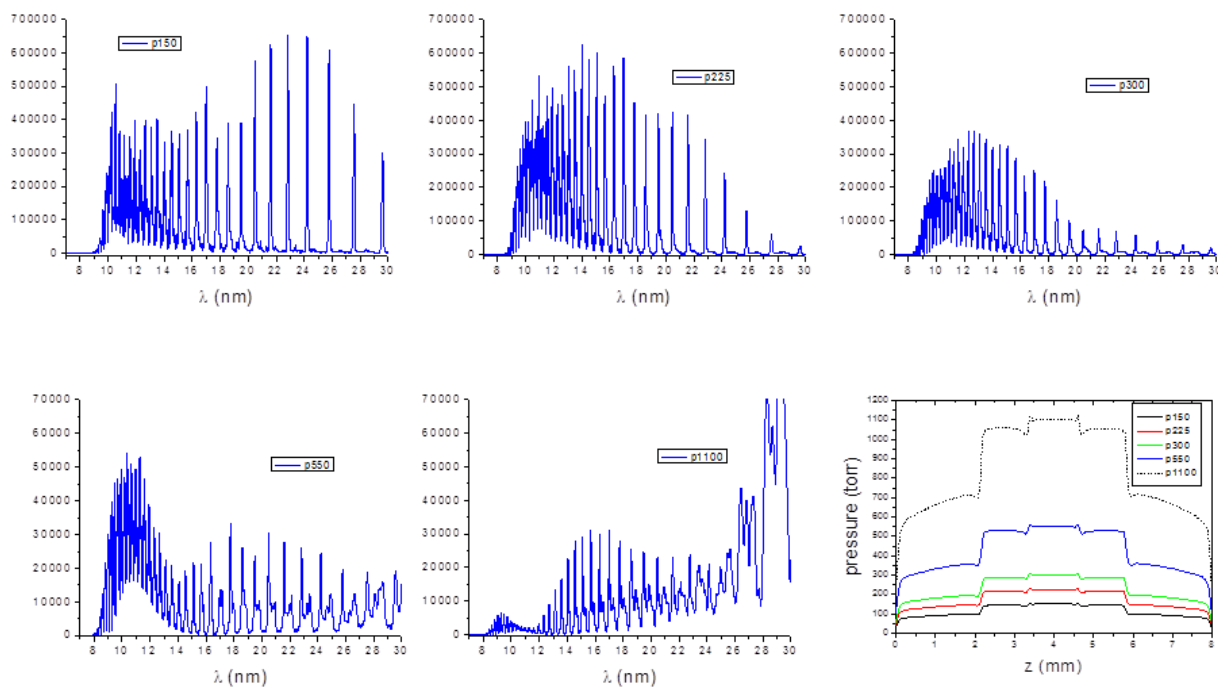


Fig. 5.1 The near field power spectra for the pressures indicated in the lower right panel.

As the vertical scale is the same in all graphs one can see that the pressure dependence is clearly evidenced in Fig. 5.1 and Fig. 5.2. The maximum yield for the near field spectra is obtained around 225 torr, although for higher harmonics (at 10-12 nm) a good region with phase matching is evidenced at 550 torr.

The far field power spectra exhibit clear differences with respect to the near field. This is because the far field takes into account also the divergence of the harmonics coming out from the near field. Not all spectral components of the near field will reach the far field. Here we must specify that the far field configuration follows exactly the experimental set-up for the 800 nm experiments. So one can conclude that the best pressure to work for this density profile is somewhere between 180 and 220 Torr which is in reasonable agreement with the experimental observations<sup>15</sup>.

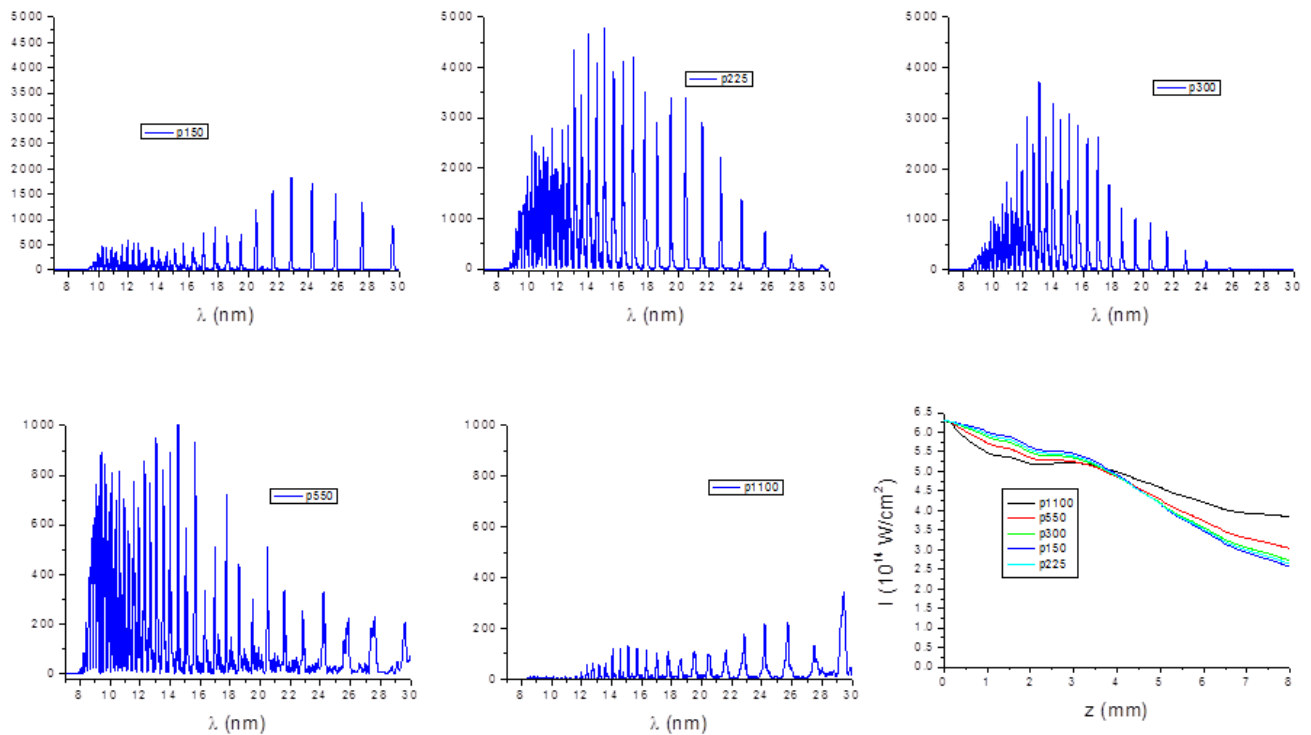


Fig. 5.2 The far field power spectra for the same pressure profiles. Note the scale five times smaller for the two highest pressures. The lower right panel shows the on-axis evolution of the peak intensity

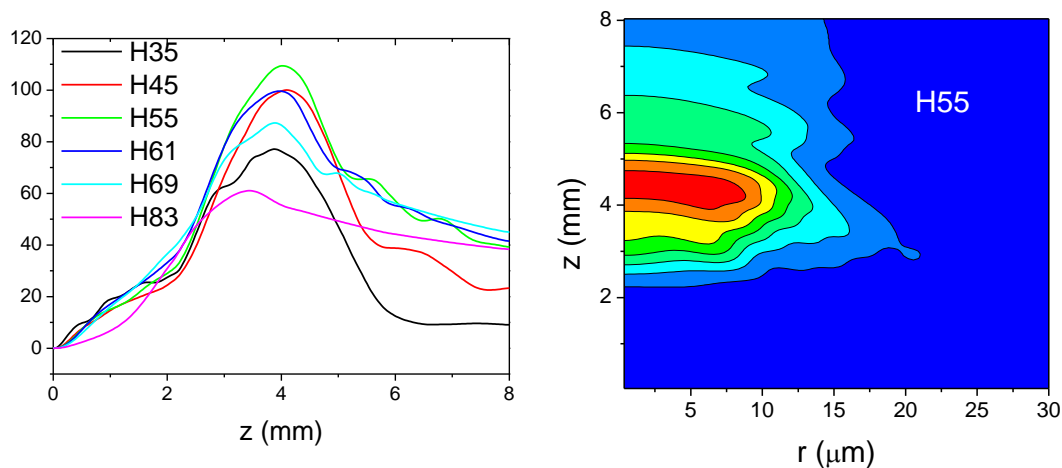


Fig.5.3 (left) Evolution of the specified harmonics along propagation in the waveguide and (right) the spatial structure of harmonic order 55 (H55) for the gas profile  $p=225$  torr.

The evolution of the driving field intensity is not very much dependent on the pressure profiles. In fact, as we will show later, the vacuum profile of the peak intensity is also close to the profiles shown in the bottom right panel of Fig. 5.2. However the phase of the laser field is much more dependent on pressure and gives rise to the dependence of the harmonic yield on pressure.

It is interesting to observe in more detail the build-up of the harmonics during propagation for the case  $p=225$  torr, which shows the best harmonic yield. Shown in Fig. 5.3 (left) is the total harmonic field built during propagation and (right) the spatial structure of harmonic H55. This is the confirmation that for the central part of the waveguide, where the pressure is 225 torr we have a phase-matched build-up of the harmonics in the XUV range from 10 to 25 nm.

### 5.2. Exploiting the gas jets

In the strategy to maximize the harmonic yield we also considered the alternative of using configurations in which jets of gas are inserted along the propagation direction. These configurations use nozzles inserted from the side of the waveguide which create jumps in the gas density, as shown in Fig. 5.4 for the case of no jets, 3 jets and 4 jets. The background pressure between the jets is from 10 to 20 torr, so that between the jets one should not expect a phase matched HHG. The advantage in this case is that we have enhanced sources of harmonics placed at different distances along the propagation and one could induce a phase matching between the harmonics generated in one jet and the ones generated in the next jet.

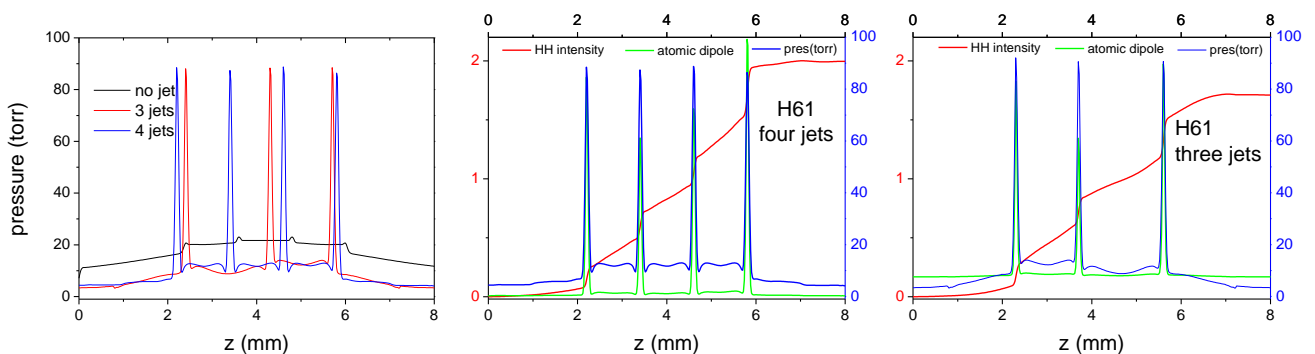


Fig. 5.4 Gas pressure, on-axis dipole intensity and harmonic field yield for order 61<sup>st</sup> along the propagation direction.

In Fig.5.4 we show some selected results obtained by modeling these three configurations. A sharp increase of the harmonic field can be seen at every jet, and this is due to the higher density which creates a jump in the polarization (see eq. 2.9). However, inside the jet one cannot estimate the condition of the phase matching. From the values for the phase matching pressure we can only say that it is below the optimum value. Between the jets we have an increase of the harmonic yield but also here the pressure is too low for a phase matched regime.

Our conclusion, for the investigated range of pressures is that using jets will contribute to increasing harmonic yield but not in a phase matched regime. Increased density of emitters will

induce the jump of the harmonic yield but especially for lower order harmonics. The results (not shown here) for higher orders show an increase in the yield in the first and second jet but a decrease of the yield in the following jets.

### 5.3. Exploiting the mode beating

When the initial radial profile  $E(r)$  of the input beam cannot be assumed as  $J_0\left(u_{11}\frac{r}{a}\right)$ , and in most experiments this is the case, the decomposition of this profile on the normal modes includes also higher order modes  $J_0\left(u_{1m}\frac{r}{a}\right)$ , of smaller amplitude. During propagation the interference of these modes during propagation give rise to a periodic variation of the total amplitude known as mode beating. For example the period of the beating between the lowest order modes  $E_{11}$  and  $E_{12}$  can be calculated as <sup>16</sup>:

$$\Delta z = \frac{2\pi}{\beta_{12} - \beta_{11}}$$

where the propagation constant is

$$\beta_{1m} = \frac{2\pi}{\lambda} \left[ 1 - \frac{1}{2} \left( \frac{u_{1m}\lambda}{2\pi a} \right)^2 \right]$$

For  $m=1, 2$ , so that

$$\Delta z = \frac{8\pi a^2}{\lambda(u_{12}^2 - u_{11}^2)} \quad (5.2)$$

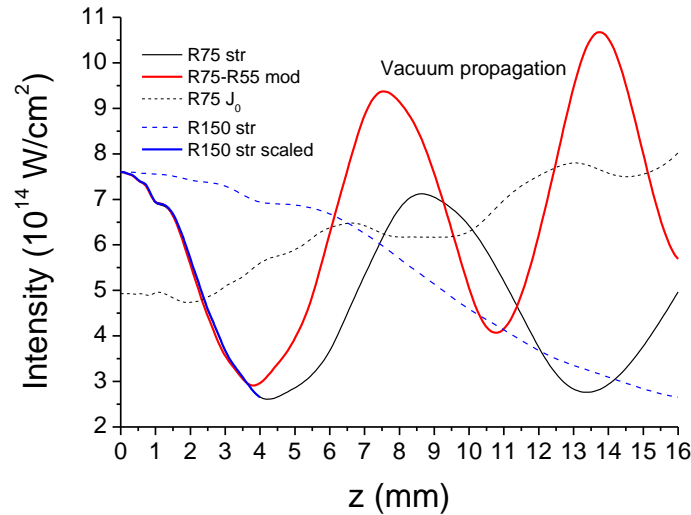


Fig 5.5 On-axis intensity for propagation in vacuum in a fiber of radius R both straight (str) and modulated (mod). The initial profile is a Gaussian but the Bessel profile  $J_0$  is also included.

As one can observe, the period of the beating depends (neglecting nonlinear effects) inversely on wavelength and directly on the square of the fiber radius. Given in Fig.5.5 is the on-axis intensity

for propagation in vacuum for a number of cases at  $\lambda=2000$  nm: we selected two fiber radii,  $75 \mu\text{m}$  and  $150 \mu\text{m}$  of straight fibers but we also considered the case of a modulated fiber in which the radius starts at  $75 \mu\text{m}$  and shrinks linearly to  $55 \mu\text{m}$  in  $16$  mm fiber length.

We first note that  $R=150 \mu\text{m}$  obeys Eq.5.2, so that the calculation for  $150 \mu\text{m}$  overlaps exactly with  $R=75 \mu\text{m}$  calculation if one shrinks by 4 times the  $z$  scale of the  $R=150 \mu\text{m}$  calculation. Second, the modulated fiber will have a variable period but follows the rule of Eq.5.2, so the period decreases, in parallel with an increase of the on-axis intensity. We also note that the case in which the initial radial profile is  $J_0\left(u_{11}\frac{r}{a}\right)$ , we do not observe the mode beating.

The mode beating was explored in this part of project development in two ways: to vary the gas density in combination with intensity variations, and to modulate the fiber diameter on a long scale distance so that to obtain a phase matched HHG due to intensity variation. We stress here that this fiber size modulation is different from the micron level variation which is proposed in the literature.

In presence of ionizing medium the basic phenomenon, mode beating, remains but the field will be modified in amplitude, phase, and step of variation. We explored several gas configurations, as shown in Fig.5.6 with the idea to combine the amplitude variation with gas density variation. However we mention that the investigations of other possibilities are still in course because the amplification of the harmonic signal shows promising results. This strategy direction is especially worth to explore for very high harmonic orders which fall in the water window region.

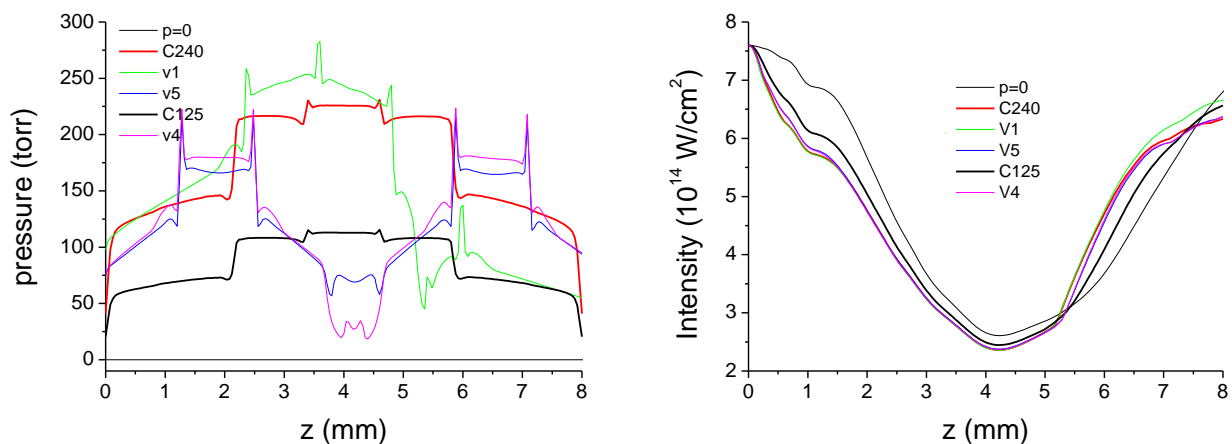


Fig.5.6 Gas configurations used for modeling (left) and corresponding on-axis intensity variation (right)

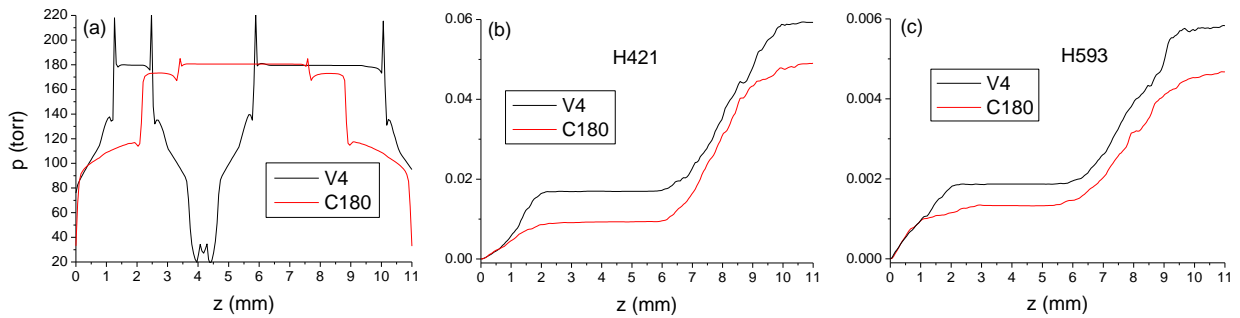


Fig.5.7 Two pressure profiles (a) and total harmonic yield for harmonic orders H421 (b) and H593 (c)

As an example we present here the comparison between the V4 configuration and the C180 configuration, both extended over 11 mm of waveguide, and both having the same plateau value of the pressure as shown in Fig. 5.7.a. The generation of two harmonic orders is shown in Fig.5.7.b and 5.7.c for XUV wavelengths of 4.75 and 3.3 nm respectively, the last one falling in the water window region. One can see that both configurations yield two intervals of increasing harmonic signal from 0 to 2 mm and from 6 to 10 mm. As the intensity variation is negligibly different we conclude that the differences are due to the variation of gas density along waveguide. A possible reason could be the steeper increase of the gas density for V4 distribution, so an effect due to the harmonic polarization.

#### 5.4. Exploiting the waveguide modulation

In the literature<sup>17</sup> the idea of fiber size modulation to induce QPM was advanced as follows: a diameter modulation of the fiber will induce a modulation of the intensity which in turn will

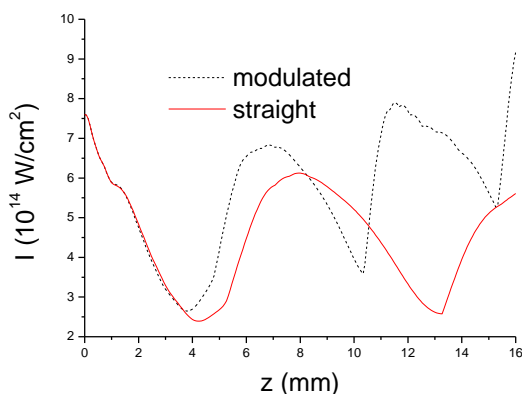


Fig. 5.8 On-axis intensity for a straight and modulated fiber.

modulate the intensity and phase of the dipole, avoiding at some point the destructive interference between the dipole and the previously created harmonic field. Our simulation on this direction led us to the conclusion that this is possible only for very short (sub-millimeter) propagation distances, so that a variable step of the modulation would be necessary.

Our approach here is different. We assume a fiber modulation at macroscopic level (along several millimeters of propagation) which will induce an intensity modulation different from that of the straight fiber. If the fiber size

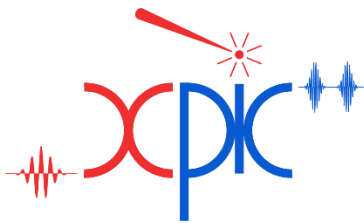
decreases the step of the modulation will also decrease, as shown in Fig. 5.5 for vacuum propagation. The size variation is assumed to be linear which is convenient from the point of view of fabrication. The QPM exploiting size modulation was theoretically proposed<sup>18</sup> and experimentally investigated<sup>19</sup> for a Gaussian profile and for an Airy profile. This last case was analyzed because for maximal extracted pulse energy from the laser the transverse profile (before focusing) is a top hat one.



Fig 5.9 Total harmonic field variation for the harmonics specified on the panels. Left column “low” order, right column high order harmonics

We explored a number of configurations assuming a Gaussian profile but other parameters were varied such as the fiber size and length, gas pressure and pulse energy and duration. We only present here one result to illustrate the method. For a straight (150  $\mu\text{m}$  diameter) and modulated (from 150 to 110  $\mu\text{m}$ ) fiber we show the results in Fig. 5.8 the variation of the on-axis intensity, demonstrating the variation of the intensity modulation step and its increase along propagation.

The harmonic field build-up follows the variation of the intensity, but this dependence is different for low or high order harmonics. Here the calculation was done for a driving field at 2000 nm,



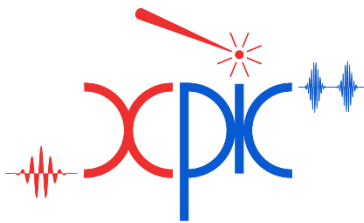
This project has received funding from the European Union's Horizon 2020 research and innovation programme under grant agreement No 964588.

assuming a gas distribution in Fig. 5.6, so that low order harmonics means here around order 200 and high order means orders over 500 (XUV wavelength around 4 nm) to reach the water window.

Shown in Fig. 5.9 is the variation of total harmonic yield for selected harmonics over a length of 16 mm, corresponding to the intensity variations in Fig.5.8.

One can observe that for harmonic orders around 200 the yield is not in favor of one or another configuration. The local maxima which are observed are due to the driving field intensity variations (see Fig. 3.7) at larger distances from the fiber axis, which generate contributions to the XUV field. For high orders the behavior is cleaner, as they are generated only close to the axis. Also the modulated fiber yields higher values with respect to the straight fiber by five to six times. This variation is connected to the intensity variations: every step of yield increase (from 6 to 8 and from 12 to 14 mm) takes place in the regions where the intensity has a smooth variation.

The present results have the potential of being up-scaled. The fiber length can be increased but also the fiber size and modulation can be modified to increase the harmonic yield.



This project has received funding from the European Union's Horizon 2020 research and innovation programme under grant agreement No 964588.

## 6. Conclusions

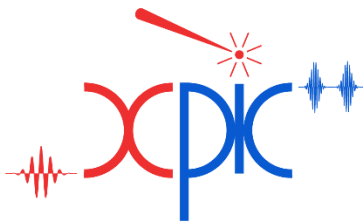
Numerical model for the ultrashort pulse propagation and XUV attosecond pulses generation in hollow core dielectric fibers was developed to cope with the experimental conditions foreseen to be used during project development.

The primary goal of the modeling was to explore the methods which can be used for generating harmonics under quasi-phase-matching conditions. These methods are known mainly for experiments in free jets or static cells so we explored their feasibility in the guided structures. In the end, the role of these modeling was to offers design indications for the chip configuration, laser parameters and gas distribution inside the chip.

The methods to achieve QPM in HHG experiments were numerically scanned via extensive modeling, and for two driving wavelengths (800 nm and 2000 nm) which are and respectively will be used in the experiments. The methods and the obtained results are listed below:

1. We found the static pressure for which phase matching occurs in our experimental conditions; this was done for 800 nm case as we have already experimental data; the pressure range in which we found phase matching agrees with what we found in the literature.
2. We studied the pressure profiles generated by a series of gas jets in the channel, as previously fabricated in the lab for HHG experiments with 800 nm. We observed the harmonic yield evolution which follows the gas density along the channel, but concluded that phase matching does not occur in these configurations.
3. Mode beating in the fiber cannot be avoided when using Gaussian beams as input beams, but can be used as a tool to periodically enhance the harmonic yield. It is one of the ways we identified for further development of the HHG under QPM conditions. As an alternative the mode beating can be combined with gas density modulations
4. Fiber diameter modulations over large steps were found to change the periodicity of the driving amplitude and phase modulation. It was demonstrated that the harmonic yield is enhanced by five to six times when the diameter was continuously varying compared to the fiber with constant diameter. This effect is of interest because it was put in evidence for 2000 nm driving pulse and has its maximum for orders around 550, which falls in the water window.

The last parameters we mentioned, namely fiber diameter, fiber diameter variation and gas density variations can induce favorable modulations of the driving field amplitude and phase over long distances and can generate harmonics in the desired range of wavelengths. We



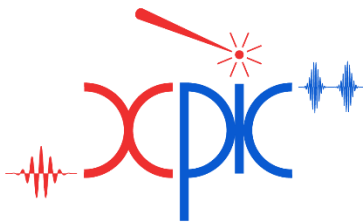
This project has received funding from the European Union's Horizon 2020 research and innovation programme under grant agreement No 964588.

cannot give at this moment a recipe for a final optimized configuration but we can show the direction of investigation from the experimentally point of view.

One essential aspect in implementing a specific configuration is to have reliable tools for fiber characterization, gas density and propagation diagnostics, tools which can give information about the evolution of the field intensity along the channel. As shown in the literature, one alternative is to *measure the fluorescence emission of the medium as a function of propagation direction*. Once this measured quantity is in agreement with numerical calculations one can extract from the calculations the characteristics of the harmonic field: range of spectral and temporal emission, intensity and phase profile, divergence, and so on, namely all important parameters to advance further on in designing the whole configuration of the chip.

## 7. References

1. Brabec, T. & Krausz, F. Intense few-cycle laser fields: Frontiers of nonlinear optics. *Rev. Mod. Phys.* **72**, 545–591 (2000).
2. Corkum, P. B. Plasma perspective on strong field multiphoton ionization. *Phys. Rev. Lett.* **71**, 1994 (1993).
3. Tosa, V., Kim, H. T., Kim, I. J. & Nam, C. H. High-order harmonic generation by chirped and self-guided femtosecond laser pulses. I. Spatial and spectral analysis. *Phys. Rev. A* **71**, 063807 (2005).
4. Tosa, V., Kim, H. T., Kim, I. J. & Nam, C. H. High-order harmonic generation by chirped and self-guided femtosecond laser pulses. II. Time-frequency analysis. *Phys. Rev. A* **71**, 63808 (2005).
5. Boyd, R. W. *Nonlinear Optics*. (Academic Press, 2003).
6. Marcatili, E. A. J. & Schmeltzer, R. A. Hollow Metallic and Dielectric Waveguides for Long Distance Optical Transmission and Lasers. *Bell Syst. Tech. J.* **43**, 1783–1809 (1964).
7. Lewenstein, M., Balcou, P., Ivanov, M. Y., L'Huillier, A. & Corkum, P. B. Theory of high-harmonic generation by low-frequency laser fields. *Phys. Rev. A* **49**, 2117–2132 (1994).
8. Balcou, P., Salieres, P., L'Huillier, A. & Lewenstein, M. Generalized phase-matching conditions for high harmonics: The role of field-gradient forces. *Phys. Rev. A* **55**, 3204–3210 (1997).
9. Magni, V., Cerullo, G. & De Silvestri, S. High-accuracy fast Hankel transform for optical beam propagation. *J. Opt. Soc. Am. A* **9**, 2031 (1992).
10. Ammosov, M. V., Delone, N. B. & Krainov, V. P. Tunnel ionization of complex atoms and of atomic ions in an alternating electromagnetic field. *Sov. Phys. JETP* **64**, 1191 (1986).



This project has received funding from the European Union's Horizon 2020 research and innovation programme under grant agreement No 964588.

11. Scrinzi, A., Geissler, M. & Brabec, T. Ionization above the coulomb barrier. *Phys. Rev. Lett.* **83**, 706–709 (1999).
12. Poletti, F. & Horak, P. Description of ultrashort pulse propagation in multimode optical fibers. *J. Opt. Soc. Am. B* **25**, 1645 (2008).
13. Chapman, R. T. *et al.* Modal effects on pump-pulse propagation in an Ar-filled capillary. *Opt. Express* **18**, 13279 (2010).
14. Naumov, A. N. *et al.* Pressure control of phase matching in high-order harmonic generation in hollow fibers filled with an absorbing weakly ionizing gas. *J. Opt. Soc. Am. B* **18**, 811 (2001).
15. Ciriolo, A. G. *et al.* High-order harmonic generation in a microfluidic glass device. *J. Phys. Photonics* **2**, 024005 (2020).
16. Pfeifer, T. & Downer, M. C. Direct experimental observation of periodic intensity modulation along a straight hollow-core optical waveguide. *J. Opt. Soc. Am. B* **24**, 1025 (2007).
17. Gibson, E. A. *et al.* Coherent soft x-ray generation in the water window with quasi-phase matching. *Science (80-. )*. **302**, 95–98 (2003).
18. Dromey, B., Zepf, M., Landreman, M. & Hooker, S. M. Quasi-phasematching of harmonic generation via multimode beating in waveguides. *Opt. Express* **15**, 7894 (2007).
19. Zepf, M., Dromey, B., Landreman, M., Foster, P. & Hooker, S. M. Bright quasi-phase-matched soft-X-ray harmonic radiation from argon ions. *Phys. Rev. Lett.* **99**, 1–13 (2007).